Effects of Aeroelasticity on Buffet Onset of Mach 0.8 Transonic Truss-Braced Wing

Juntao Xiong*
KBR Wyle, Inc., Moffett Field, CA 94035
Nhan Nguyen†
NASA Ames Research Center, Moffett Field, CA 94035

This paper presents a buffet simulation of the Mach 0.8 Transonic Truss-Braced Wing (TTBW) aeroelastic model using CFD solver FUN3D. A jig twist optimization is performed to obtain a flight optimized jig twist for the flexible Mach 0.8 TTBW model. A series of Delayed Detached Eddy Simulation (DDES) aeroelastic simulations has been conducted at Mach number 0.8 and altitude 40, 000 ft using a structural damping of 2% **to compare the pitch break prediction and the buffet behavior for the TTBW aeroelastic model. The unsteady pressure begins to grow at angle of attack of** 4.0°**, which might indicate the buffet onset, and rises one order of magnitude larger at angle of attack of** 4.5°**. In contrast, the buffet onset for the TTBW 1g model appears to be at the angle of attack of about** 3.5°**. The delay in the buffet onset of the aeroelastic model is due to the load relief from the aeroelastic effect.**

I. Introduction

Stability is one of the important requirements in aircraft design. Stable aircraft response without active feedback control is a desired attribute in transport aircraft design. In the transonic flow regime, shock wave and turbulent boundary layer interaction and flow separation induce a large scale self-sustained motion of the shock wave over the aircraft surface. This unsteady shock motion is called transonic buffet. The unsteadiness of the shock wave motion may cause overloading of the structures and might induce the aircraft instability issues and structural mode interactions.. A good understanding and prediction of transonic buffet flow behavior is important for a new generation aircraft design as modern transport aircraft are designed for higher cruise Mach number.

The Subsonic Ultra Green Aircraft Research (SUGAR) Transonic Truss-Braced Wing (TTBW) aircraft concept is a Boeing-developed N+3 aircraft configuration funded by NASA Aeronautics Research Mission Directorate (ARMD) Advanced Air Transport Technologies (AATT) project.[1,2,3] The Mach 0.8 Transonic Truss-Braced Wing (TTBW) aircraft shown in Figure 1 is designed to be aerodynamically efficient by employing a large aspect ratio. The stability characteristics and buffet behavior of the rigid TTBW 1g OML have been studied previously.[4,5,6,7] However, the aeroelastic effects might change the aircraft loading distribution especially near the wing outboard region, which might alter the aerodynamic performance, stability characteristics, and buffet behavior at high angle of attack.

In this paper, an unsteady buffet simulation of the Mach 0.8 TTBW aeroelastic model is performed to investigate the buffet behavior at high angles of attack. Firstly, a jig twist optimization is performed to obtain a flight optimized jig twist for the flexible Mach 0.8 TTBW model. Then, a series of Delayed Detached Eddy Simulation (DDES) aeroelastic simulations is conducted at Mach number 0.8 and altitude 40, 000 ft using a structural damping of 2% to compare the pitch break prediction and the buffet behavior for the TTBW aeroelastic model. The simulation results are compared with TTBW 1g model to investigate the aeroelastic effects on buffet behavior at high angles of attack.

*Aerospace Engineer, Intelligent System Division, juntao.xiong@nasa.gov, AIAA Member
†Senior Research Scientist and Technical Group Lead, Intelligent Systems Division, nhan.t.nguyen@nasa.gov, Associate Fellow AIAA

Figure 1 Boeing SUGAR Mach 0.8 Transonic Truss-Braced Wing (TTBW) Aircraft Concept

II. Computational Approach

A. Numerical Code

The computational fluid dynamics code used in this study is FUN3D,[8,9] which solves the unsteady three-dimensional Navier-Stokes equations on mixed-element grids using a vertices-centered finite-volume method. Information exchange for flow computation on different partitions using multiple CPUs is implemented through the MPI (Message Passing Interface) protocol. It employs an implicit upwind algorithm in which the inviscid fluxes are obtained with a flux-difference-splitting scheme. At interfaces delimiting neighboring control volumes, the inviscid fluxes are computed using an approximate Riemann solver based on the values on either side of the interface. The Roe flux difference splitting[10] is used in the current study. For second-order accuracy, interface values are obtained by extrapolation of the control volume centroidal values, based on gradients computed at the mesh vertices, using an unweighted least squares technique. The Venkatakrishnan[11] limiter is used in the current study to limit the reconstructed values when necessary. In this study the tetrahedral mesh with prism layers are used. In FUN3D, for tetrahedral meshes, the full viscous fluxes are discretized using a finite-volume formulation in which the required velocity gradients on the dual faces are computed using the Green-Gauss theorem. The solution at each time-step is updated with a backwards Euler time-differencing scheme. At each time step, the system of equations is approximately solved with either a multi-color point-implicit procedure or an implicit-line relaxation scheme. Local time-step scaling is employed to accelerate convergence to steady-state. To model turbulent flows, the one-equation model of Spalart-Allmaras[12] (S-A) is used in this study. The static aeroelastic simulation module in FUN3D is used for the aeroelastic simulation.

B. Computational Model and Grid

Figure 2 illustrates the Mach 0.8 TTBW geometry. Figure 3 shows the surface meshes of the geometries. The volume meshes are comprised of tetrahedral elements and a prism layer near the wall. The mesh size is about 192 million nodes for the Mach 0.8 TTBW full model. The prism layer is used to resolve the turbulent boundary layer. The $y+$ of the first cell from the wall is less than 1.

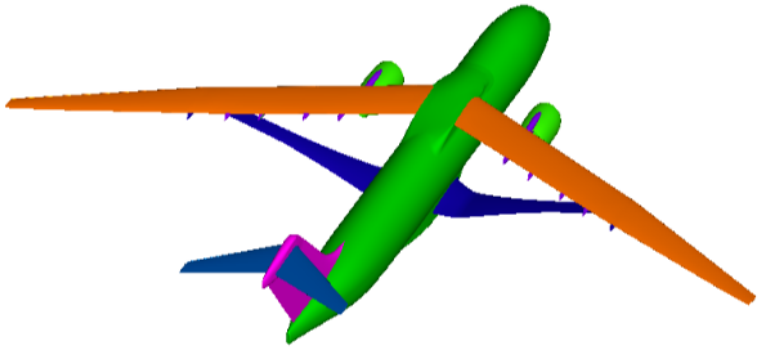

Figure 2 Mach 0.8 TTBW Aircraft Geometries.

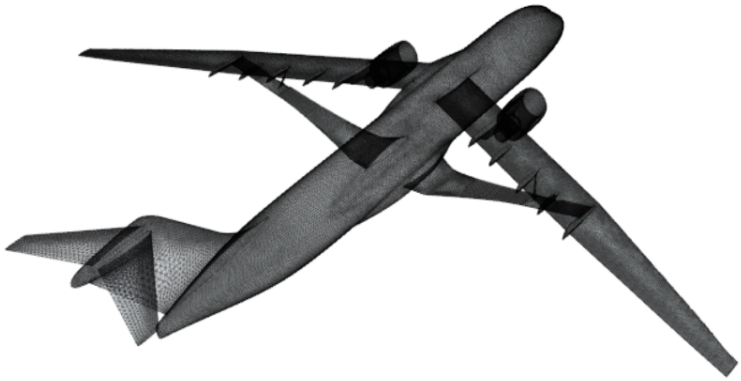

Figure 3 Mach 0.8 TTBW Aircraft CFD Meshes.

C. Aeroelastic Simulation

A NASTRAN finite-element model (FEM) of the Mach 0.8 TTBW is available from Boeing. The NASTRAN FEM comprises a detail structural model of the wing and struts, a shell structural model of the fuselage section that joins with the wing, and a beam-stick model of the rest of the fuselage and the tail empennage. This is shown in Figure 4. To reflect the estimated cruise gross weights the fuel model in the Boeing NASTRAN model has been updated. The revised NASTRAN model is used to extract mode shapes for the aeroelastic analysis for the Mach 0.8 TTBW aircraft. Figure 5 shows the mode shapes of the first six non-rigid body modes.

The static aeroelastic simulation module in FUN3D is used for the aeroelastic simulation. The mode shapes are extracted from Boeing NASTRAN model with 50% fuel. Figure 6 shows the first six non-rigid body mode displacements which are interpolated from the NASTRAN mode shapes.

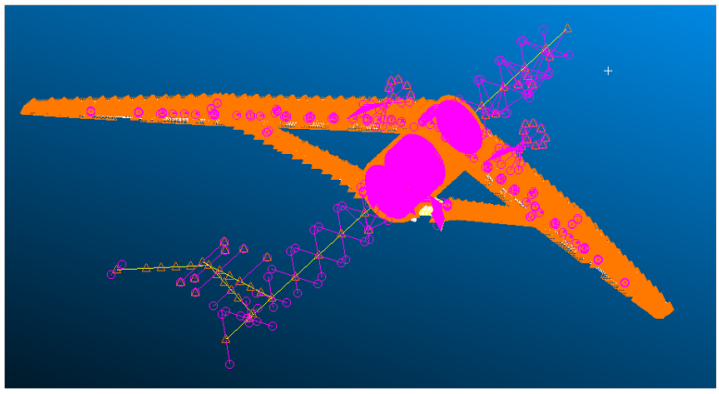

Figure 4 Boeing Mach 0.8 NASTRAN Finite-Element Model

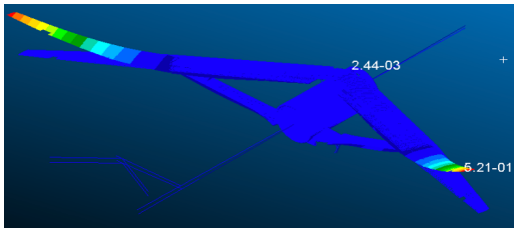

(a) 1st Mod

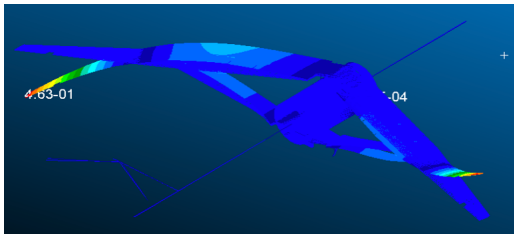

(b) 2nd Mode

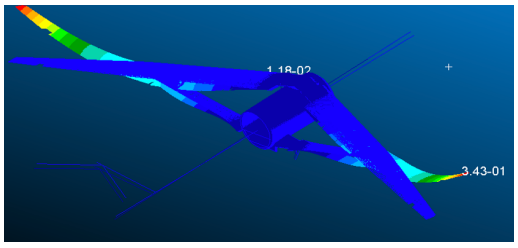

(c) 3rd Mode

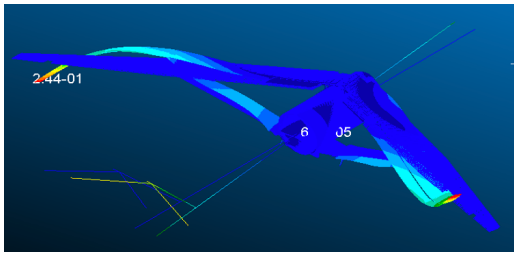

(d) 4th Mode

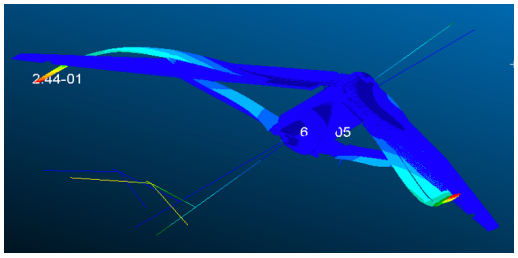

(e) 5th Mode

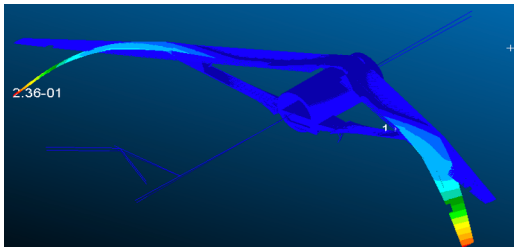

(f) 6th Mode

Figure 5 Boeing Mach 0.8 TTBW NASTRAN Mode Shapes for 50% Fuel.

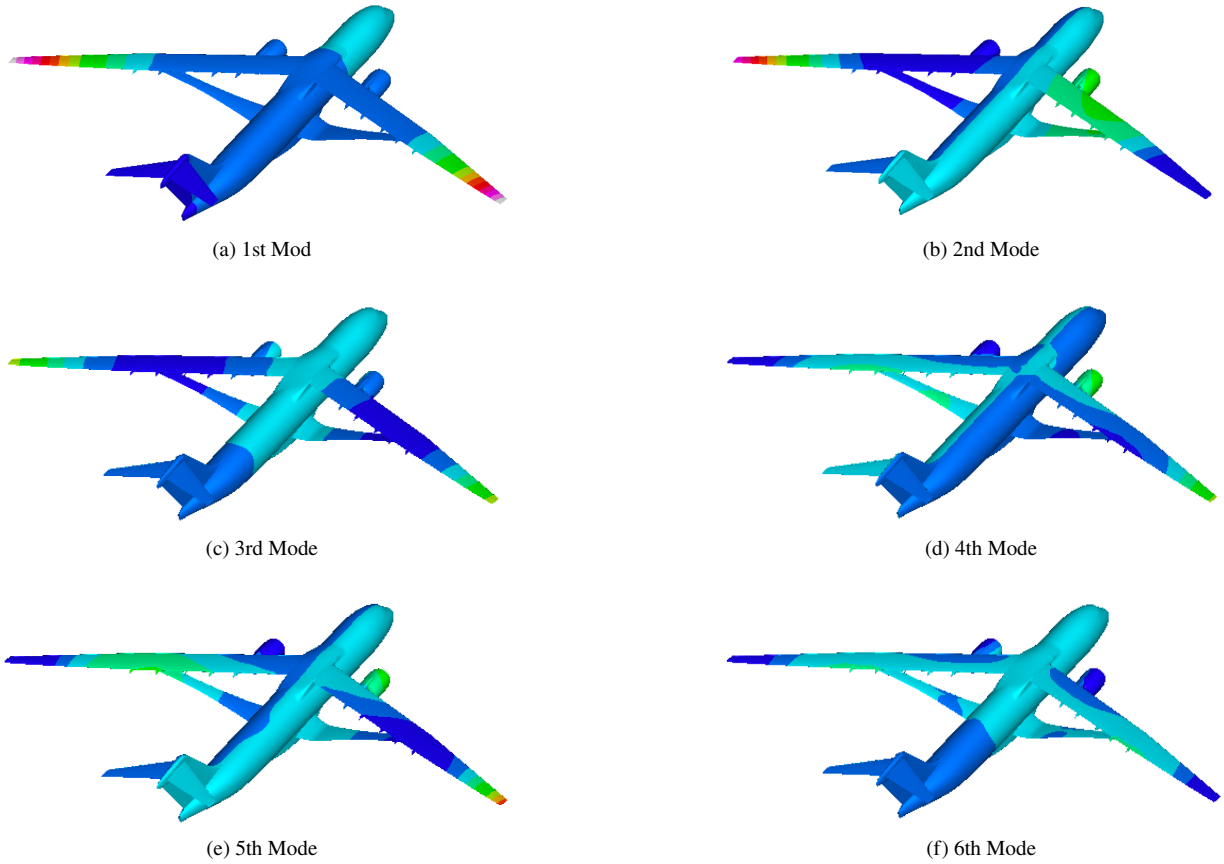

(a) 1st Mod

(b) 2nd Mode

(c) 3rd Mode

(d) 4th Mode

(e) 5th Mode

(f) 6th Mode

Figure 6 Mach 0.8 TTBW Mode Displacement Contours for 50% Fuel.

III. Jig Twist Optimization

The wind tunnel jig shape OML geometry is a jig shape designed for a wind tunnel model. Therefore, it does not properly account for the wing aeroelastic wash-out twist for the full-scale vehicle at the design flight condition. Thus, the wind tunnel jig shape model is suitable for comparisons to wind tunnel data, but not necessarily suitable for generating a model of full-scale aerodynamic performance. An optimization study is conducted to obtain a flight-optimized jig twist for the Mach 0.8 TTBW configuration.

The goal of the optimization scheme is to minimize the drag coefficient of the aero-structural model of the jig shape geometry for the TTBW aircraft at the design flight condition. The cost function is defined as:

$$J(\alpha, c) = C_D, \tag{1}$$

while subject to the design lift and zero pitching moment constraints. Design variables are the coefficients of a shape function $c = [c_1, ..., c_N]$ which parameterize the jig twist as:

$$\theta(y) = \theta_0(y) + \sum_{i=1}^{N} c_i \phi_i(y), \tag{2}$$

where $\theta(y)$ represents the jig twist distribution along the spanwise direction, $\theta_0(y)$ is the initial jig twist distribution along the spanwise direction, corresponding to the wind tunnel optimized twist model, and $\phi_i(y)$ is a shape function of degree i. Shape functions are utilized in order to limit the number of design variables for optimization as well as provide a smoother converged optimized jig twist distribution. In this study the $5^t h$ order of Chebyshev polynomial is used as the shape function. Figure 7 shows the Chebyshev polynomial shape functions.

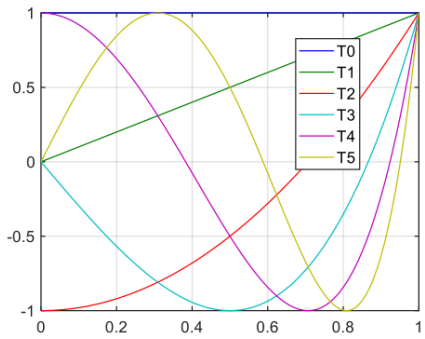

Figure 7 Chebyshev Polynomial Shape Functions

The steepest descent algorithm for updating the design variables can be represented by the following equations:

$$c_{i_{k+1}} = c_{i_k} - \epsilon \cdot \frac{\partial J}{\partial c_i}. \tag{3}$$

Here, the design variable at iteration k is updated based on the partial derivative of the cost function with respect to the design variable, which is calculated using a small-perturbation, second-order central difference scheme, and ϵ is a step size term.

The optimization procedure begins by initializing both the TTBW geometry and the parameterization of the jig twist. A baseline aero-structural solution is established by the wind tunnel jig twist model. A gradient is established based on the effect of the small perturbations such that the design variables can be updated relative to their respective cost function partial derivatives. This small perturbation iterative procedure is repeated until the cost function converges.

Two different optimizations are performed. The first one includes the angle of attack as design variable. This optimization was conducted in a previous study[13] to find a jig twist at a new angle of attack that minimizes the absolute drag. The other one constrains the angle of attack equal to the trim angle of attack of the TTBW 1g OML. The jig twist optimization produces two different flight optimized jig twist profiles as shown in the Figure 8. Figure 9 shows the pressure contour comparison of the 1g OML, flight optimized jig twist I without the angle of attack constraint and flight optimized jig II with the angle of attack constraint. The aerodynamic parameters are presented in the Table 1.

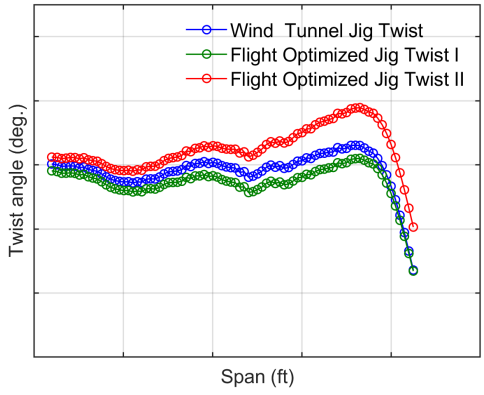

Figure 8 Flight Optimized Jig Twist Distribution.

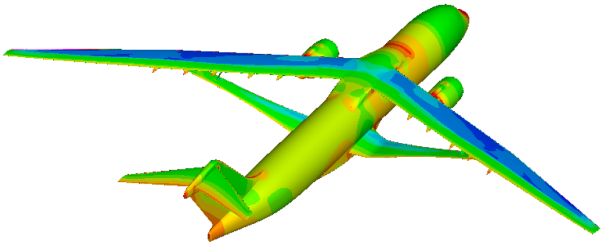

(a) 1g OML

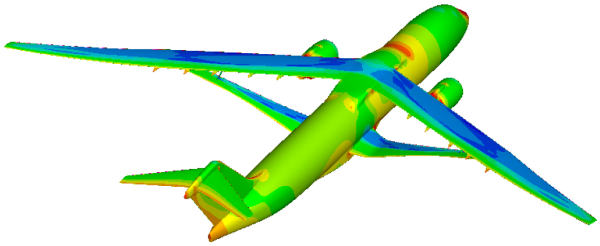

(b) Flight Optimized Jig Twist I

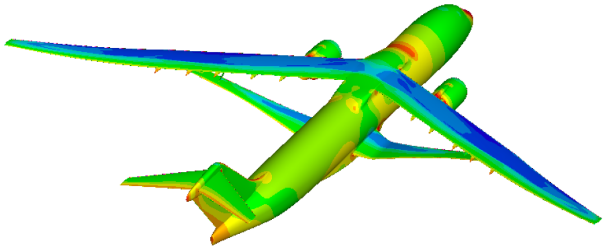

(c) Flight Optimized Jig Twist II

Figure 9 Pressure Coefficient Contour on the Mach 0.8 TTBW Surfaces at $M_\infty = 0.8$ and $C_L = 0.695$

Table 1 Jig Twist Optimization Results for $C_L = 0.695$ and $h = 40,000$ ft

Model	α_{trim}(deg.)	ΔC_D (counts)	$\Delta C_D / C_{D_{1g}}$
1g OML	1.72	-	-
Flight Optimized Jig Twist I	1.96	5.5	1.64%
Flight Optimized Jig Twist II	1.72	0.9	0.27%

Angle of attack sweeps are performed to compare the aerodynamic performance. Figure 10 shows the lift, drag, and pitching moment coefficients of the Mach 0.8 TTBW models. The flight optimized jig twist I without the angle of attack constraint causes a significant shift in the lift curve, thereby making it difficult to compare to the results of 1g OML. The lift and drag coefficients of the flight optimized jig twist II with the angle of attack constraint are in very close agreement to 1g OML simulation. The pitching moment coefficient of the flight optimized jig twist II generally agrees well with the 1g OML result at the constrained angle of attack, but differs at high angles of attack. A pitch break is observed for the flight optimized jig twist II at an angle of attack of about 3.5 degrees. In contrast, the pitch break angle of attack for the 1g OML occurs at about 2.89 degrees. The increase in the pitch break angle of attack is due to the aeroelastic relief. Since the flight optimized jig twist II is in good agreement with the 1g OML at the design trim condition, this jig twist is used to establish a new jig twist aeroelastic OML for use in unsteady buffet simulation and analysis. In the following section the flight optimized jig twist II is referred to as aeroelastic OML.

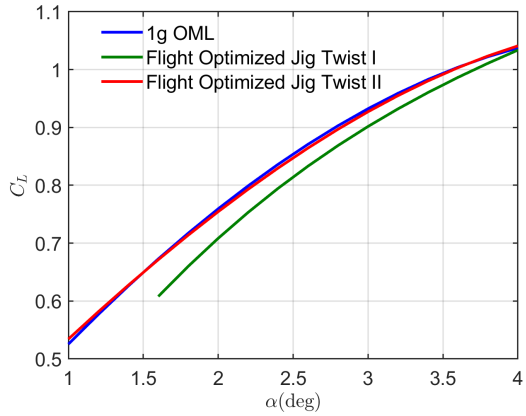

(a) Lift Curve

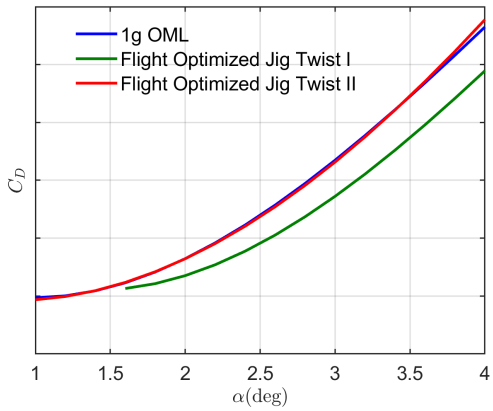

(b) Drag Curve

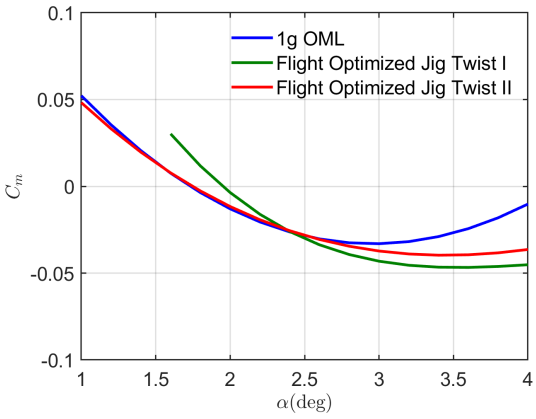

(c) Pitching Moment Curve

Figure 10 Lift, Drag, and Pitching Moment for the TTBW Models at Mach 0.8, h = 40,000ft

IV. Buffet Simulation

To further investigate the flow behavior of the developed Mach 0.8 TTBW aeroelastic model at high angles of attack unsteady Delayed Detached Eddy Simulation (DDES) is performed. In the unsteady simulation the time step is about

0.00078s for DDES.

Figure 11 shows the comparisons of the lift and pitching moment coefficients of the Mach 0.8 TTBW 1g OML and aeroelastic model using the DDES approach. Both 1g OML and aeroelastic model simulation results show the pitch break occurs at high angle of attack. Table 2 lists the angle of attack where the pitch break occurs. The pitch break of the aeroelastic OML occurs about 0.5° later than the 1g OML, which is likely due to the load relief from the aeroelastic effect.

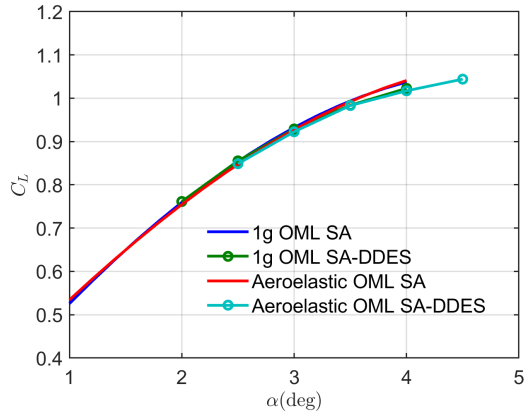

(a) Lift Curve

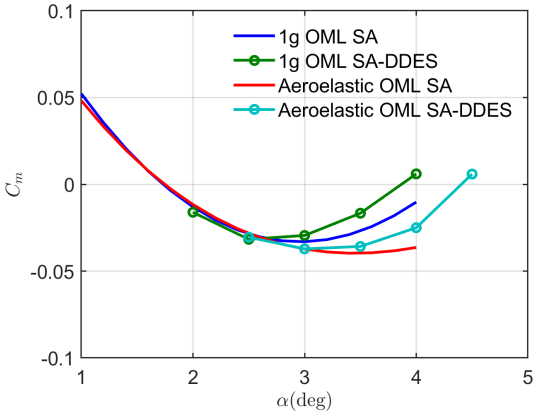

(b) Pitch Moment Curve

Figure 11 Lift and Pitching Moment for the Mach TTBW 1g OML and Aeroelastic Model at Mach 0.8 and h = 40,000ft.

Table 2 Pitch Break Angle of Attack at Mach 0.8 and $h = 40,000$ ft

Model	α(deg)
1g OML SA	2.89
1g OML SA-DDES	2.75
Aeroelastic OML SA	3.42
Aeroelastic OML SA-DDES	3.20

Figure 12 shows the instantaneous density contours for the Mach 0.8 TTBW aeroelastic model at Mach 0.8 and angles of attack 2.5°-4.5° from the DDES simulations. As the angle of attack increases, the shock wave moves to the leading edge, especially near the wing mid-span region, and displays a wavy pattern along the wing span. This is caused

by the flow separation induced by the shock wave and turbulent boundary layer interactions. Figure 13 - 17 show the the time history and frequency spectrum of the lift coefficient for the Mach 0.8 TTBW aeroelastic model at Mach 0.8 and angles of attack 2.5°-4.5° from the DDES simulations. Figure 18 - 22 show the time history and frequency spectrum of the pitching moment coefficient for the Mach 0.8 TTBW aeroelastic model. Figure 23 and Figure 24 show the comparison of the root mean square (RMS) values of the lift and pitching moment of the Mach 0.8 TTBW 1g OML and aeroelastic model. When the angle of attack is less than 4.0°, the unsteady lift remains at a small level. The unsteady lift starts growing when the angle of attack exceeds 4.0° for the Mach 0.8 TTBW aeroelastic model. However, for the Mach 0.8 TTBW 1g OML, the unsteady lift starts growing at the angle of attack of 3.5° and, then continues to rise by an order of magnitude when the angle of attack reaches 4.0°.

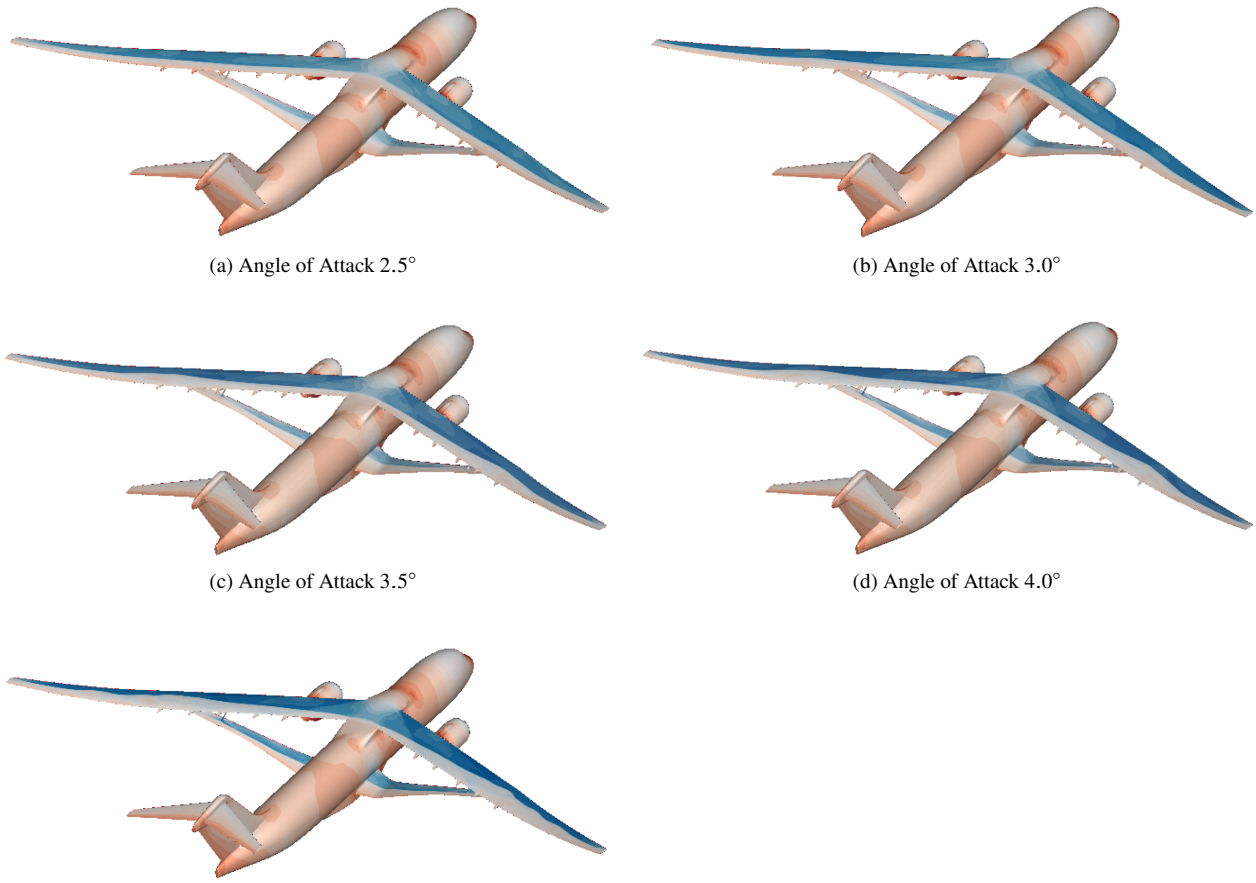

(a) Angle of Attack 2.5°

(b) Angle of Attack 3.0°

(c) Angle of Attack 3.5°

(d) Angle of Attack 4.0°

(e) Angle of Attack 4.5°

Figure 12 Instantaneous Density Contour of the TTBW Aeroelastic model at Mach 0.8 and h = 40,000ft.

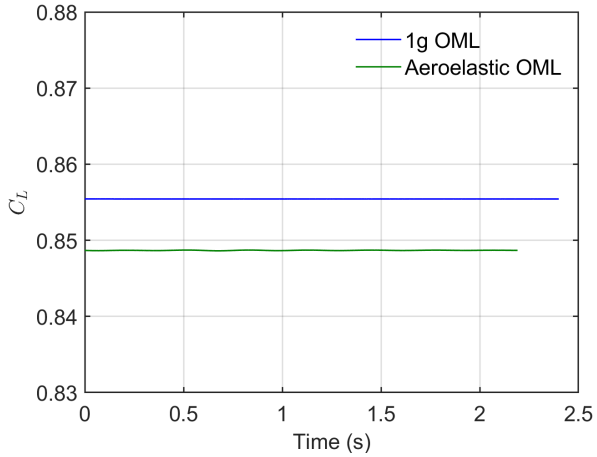

(a) Lift Time History

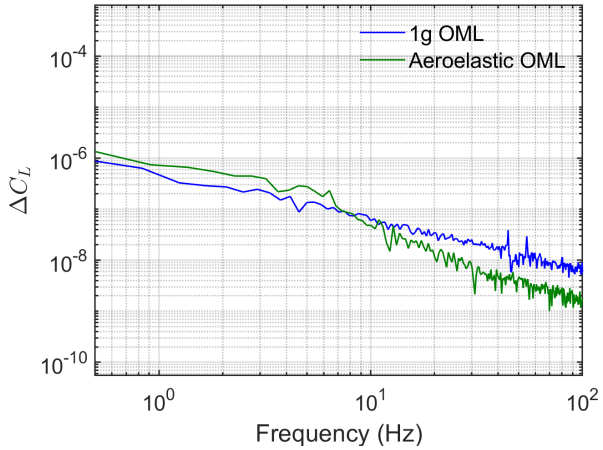

(b) Lift Spectral

Figure 13 Time History and Frequency Spectrum of Lift Coefficient at Mach 0.8, h = 40,000ft and angle of attack 2.5°**.**

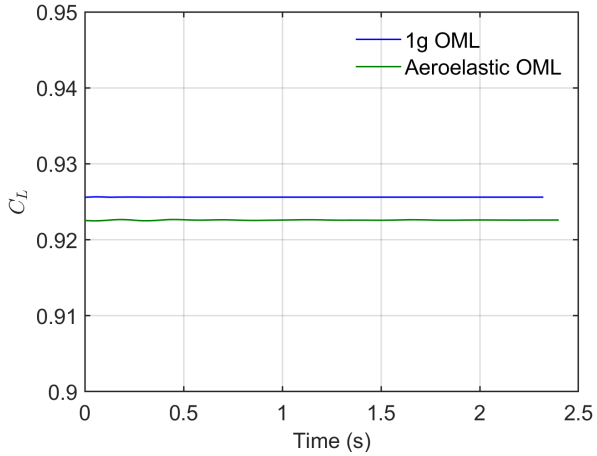

(a) Lift Time History

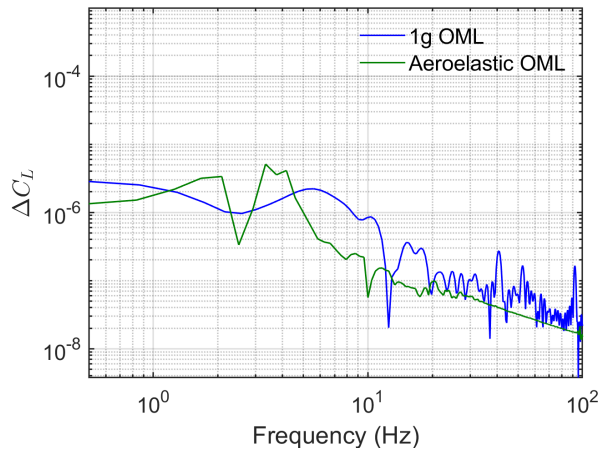

(b) Lift Spectral

Figure 14 Time History and Frequency Spectrum of Lift Coefficient at Mach 0.8, h = 40,000ft and angle of attack 3.0°**.**

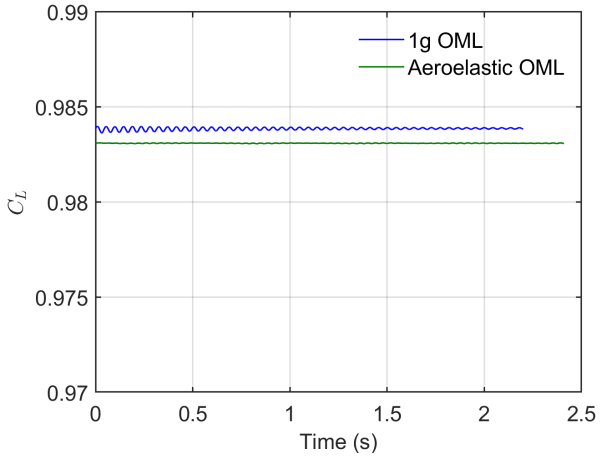

(a) Lift Time History

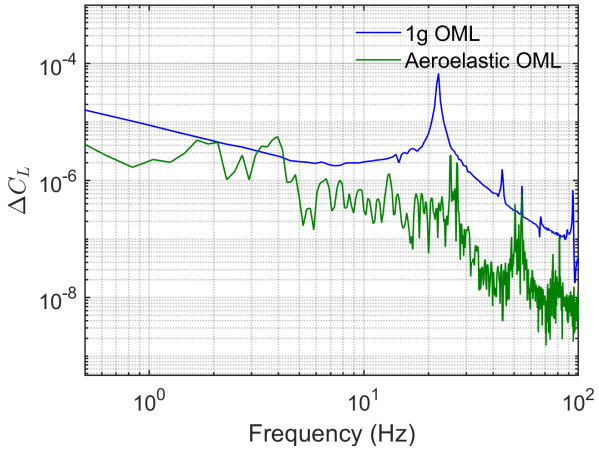

(b) Lift Spectral

Figure 15 Time History and Frequency Spectrum of Lift Coefficient at Mach 0.8, h = 40,000ft and angle of attack 3.5°**.**

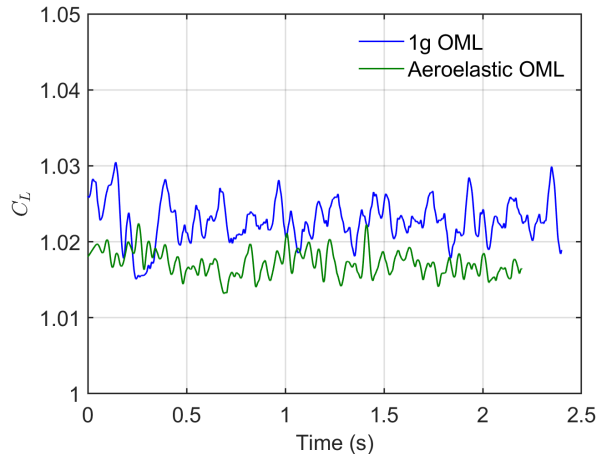

(a) Lift Time History

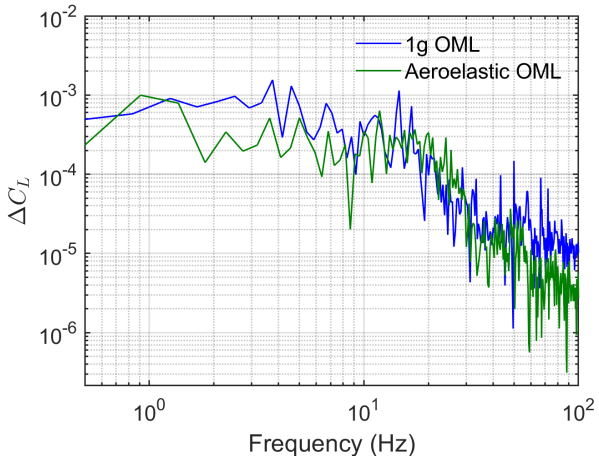

(b) Lift Spectral

Figure 16 Time History and Frequency Spectrum of Lift Coefficient at Mach 0.8, h = 40,000ft and angle of attack 4.0°**.**

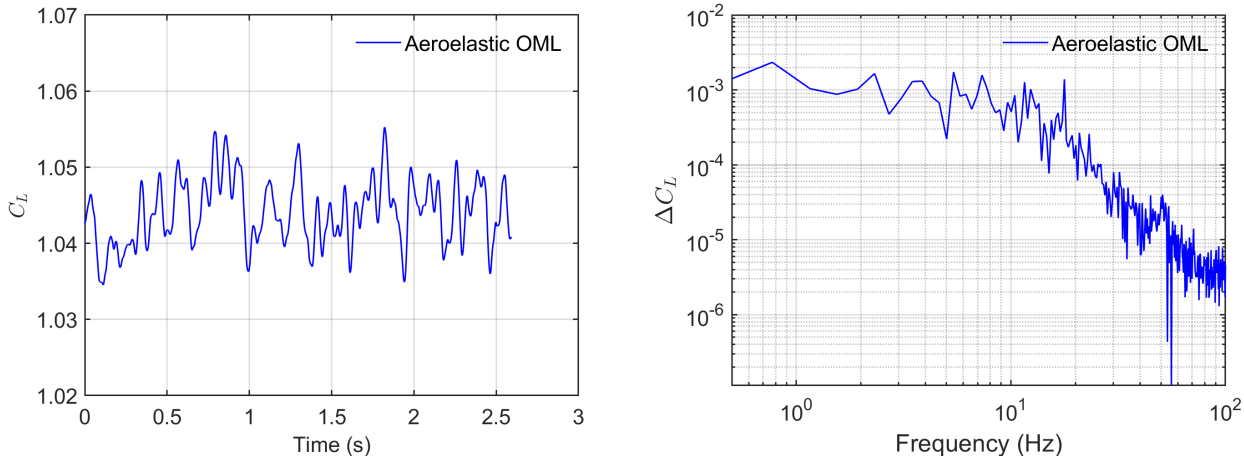

(a) Lift Time History

(b) Lift Spectral

Figure 17 Time History and Frequency Spectrum of Lift Coefficient at Mach 0.8, h = 40,000ft and angle of attack 4.5°**.**

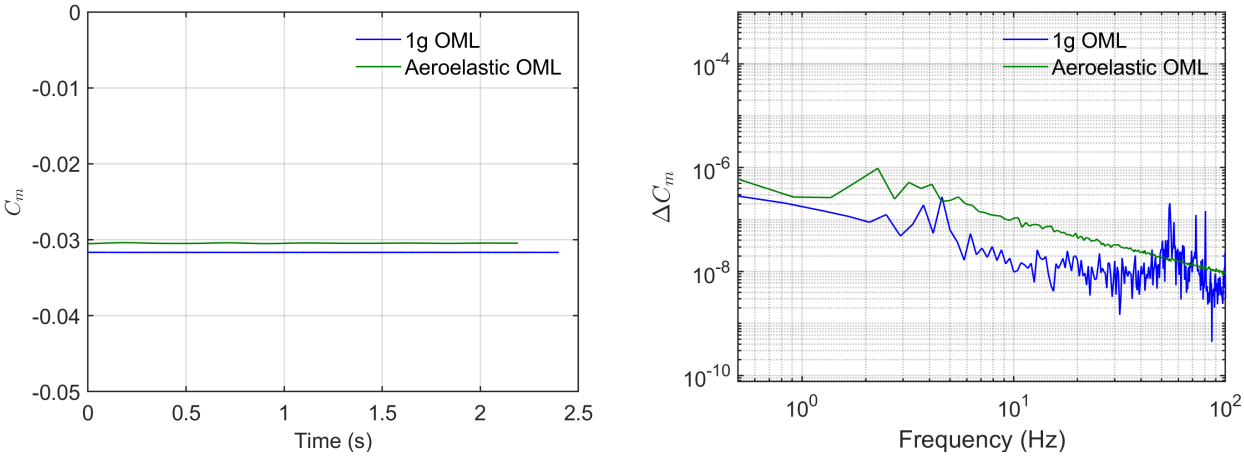

(a) Pitching Moment Time History

(b) Pitching Moment Spectral

Figure 18 Time History and Frequency Spectrum of Pitching Moment at Mach 0.8, h = 40,000ft and angle of attack 2.5°**.**

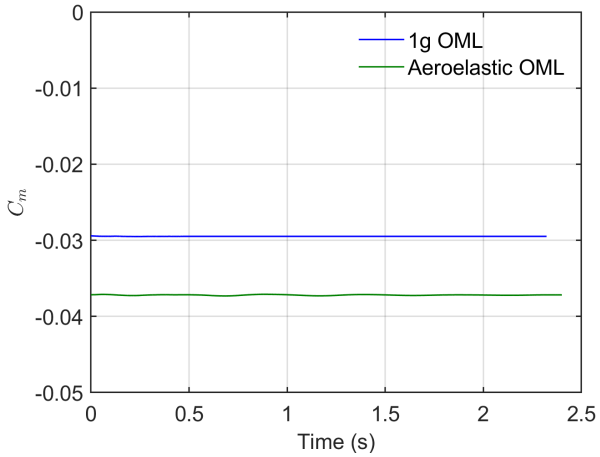

(a) Pitching Moment Time History

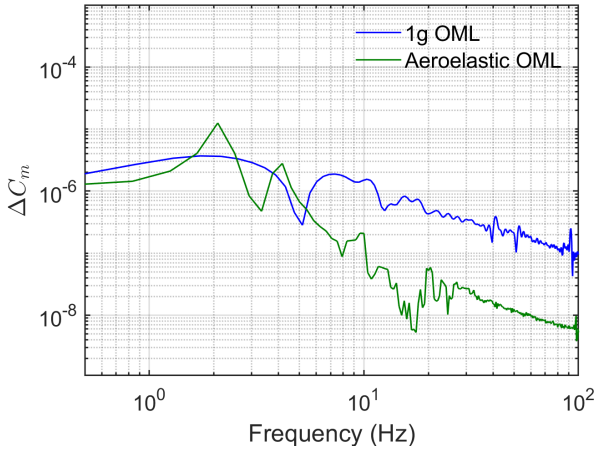

(b) Pitching Moment Spectral

Figure 19 Time History and Frequency Spectrum of Pitching Moment at Mach 0.8, h = 40,000ft and angle of attack $3.0°$**.**

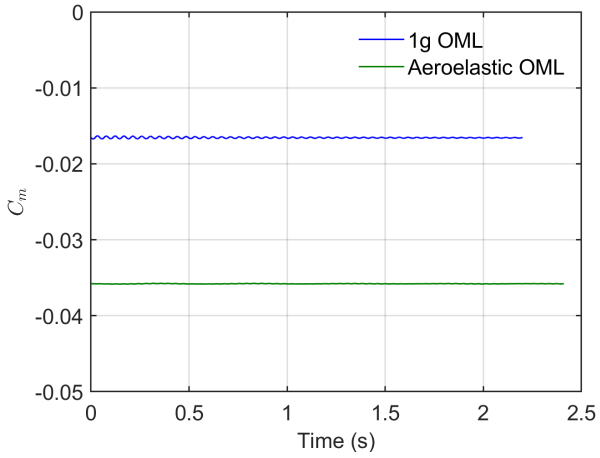

(a) Pitching Moment Time History

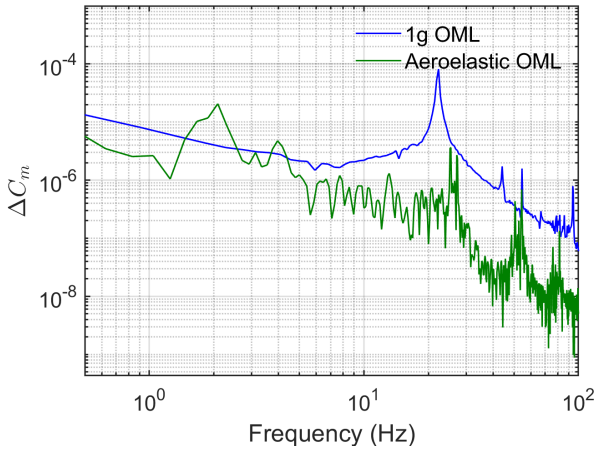

(b) Pitching Moment Spectral

Figure 20 Time History and Frequency Spectrum of Pitching Moment at Mach 0.8, h = 40,000ft and angle of attack $3.5°$**.**

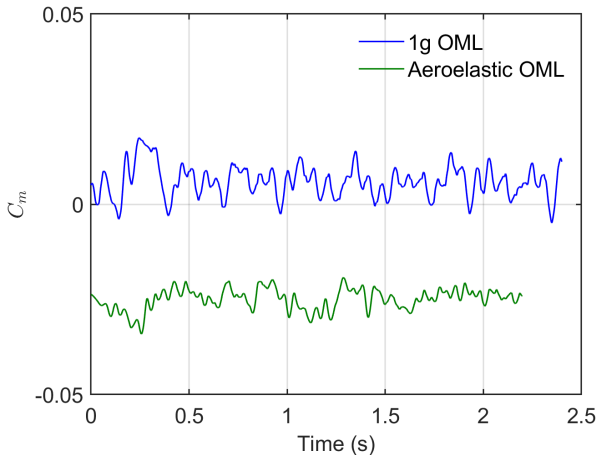

(a) Pitching Moment Time History

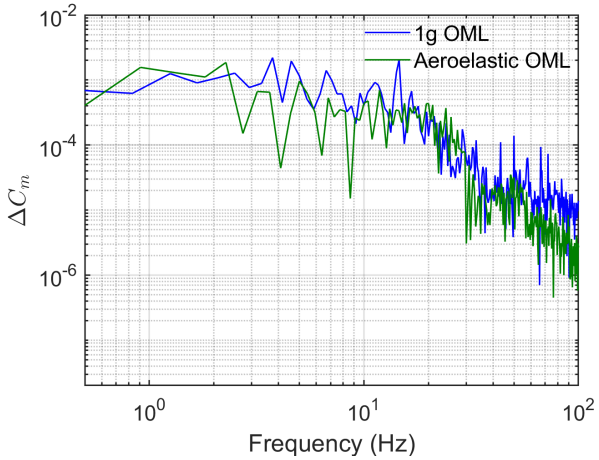

(b) Pitching Moment Spectral

Figure 21 Time History and Frequency Spectrum of Pitching Moment at Mach 0.8, h = 40,000ft and angle of attack $4.0°$**.**

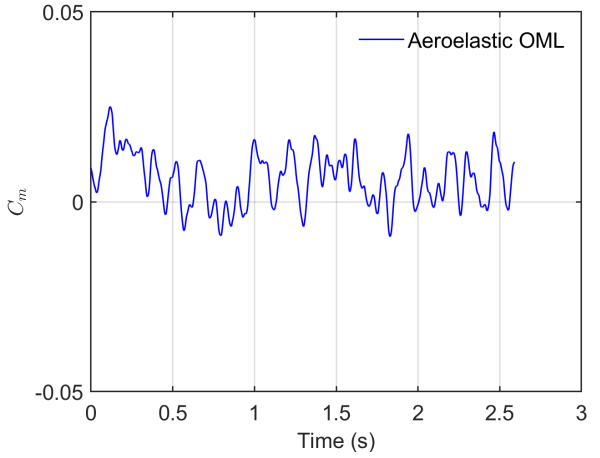

(a) Pitching Moment Time History

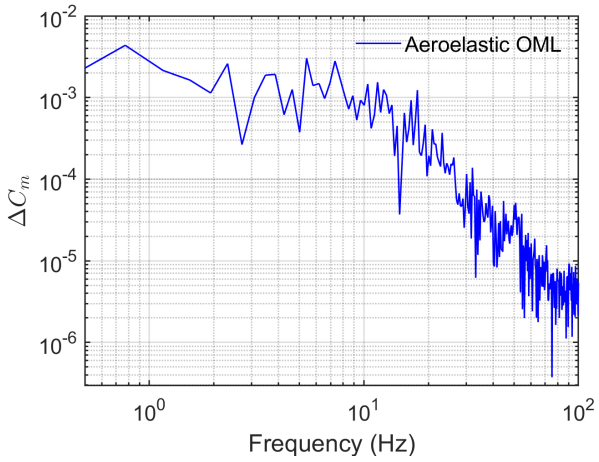

(b) Pitching Moment Spectral

Figure 22 Time History and Frequency Spectrum of Pitching Moment at Mach 0.8, h = 40,000ft and angle of attack $4.5°$**.**

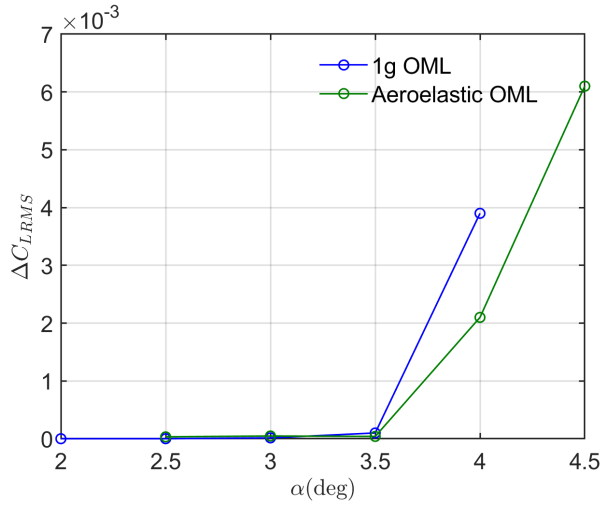

Figure 23 RMS Value of Unsteady Lift at Mach 0.8 and h = 40,000ft.

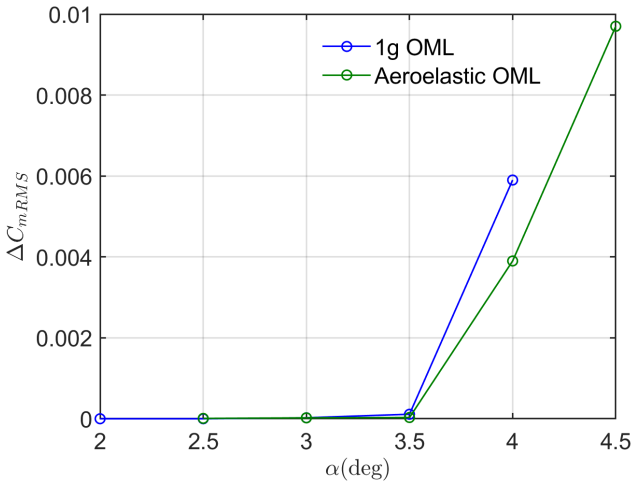

Figure 24 RMS Value of Unsteady Pitching Moment at Mach 0.8 and h = 40,000ft.

Figure 25 - 27 show the RMS values of the unsteady pressure for the Mach 0.8 TTBW 1g OML and aeroelastic model at Mach 0.8 and 40, 000 ft altitude. Figure 28 shows the peak RMS value of the unsteady pressure as a function of the angle of attack and the wing station. The red dashed line indicates the pitch break angle in the plot. At the angle of attack of 3.5° the RMS value of the unsteady pressure of the Mach 0.8 TTBW 1g OML begins to grow near the wing mid-span, which might indicate the buffet onset. As the angle of attack reaches 4.0°, the RMS value of the unsteady pressure increases by an order of magnitude, marked by a high unsteady pressure region that spans from the wing mid-span to the wing tip. However, for the Mach 0.8 TTBW aeroelastic model, the RMS value of the unsteady pressure remains almost zero at the angle of attack of 3.5°. The RMS value of the unsteady pressure begins to grow at angle of attack of 4.0° near the wing mid-span, which might indicate the buffet onset. As the angle of attack reaches 4.5°, the RMS value of the unsteady pressure continues to increase and the high unsteady pressure region expands in the entire outboard wing from near the mid-span to the wing tip.

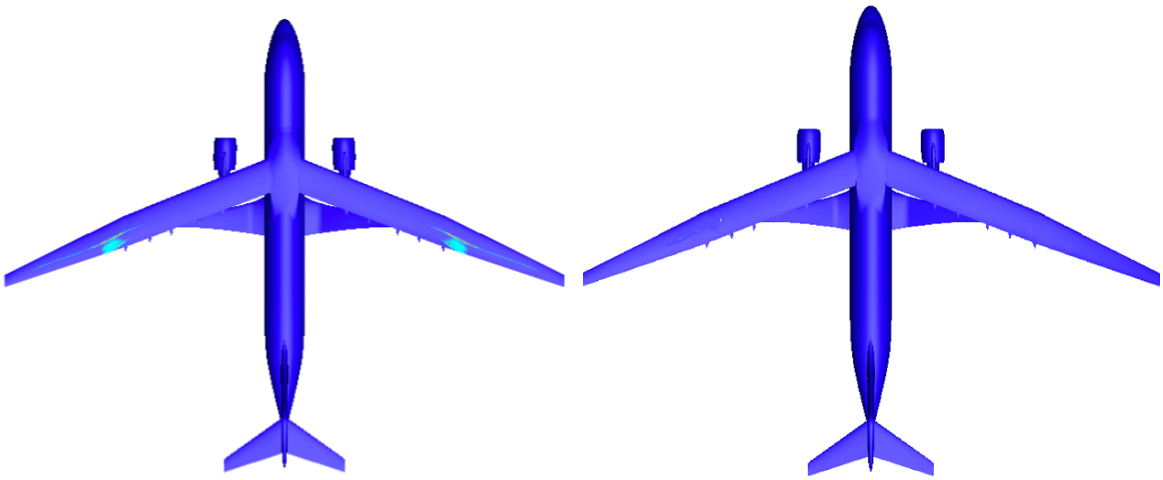

(a) 1g OML (b) Aeroelastic OML

Figure 25 RMS Value of Unsteady Pressure of the Mach 0.8 TTBW 1g OML and Aeroelastic mode at Mach 0.8, h = 40,000ft and angle of attack $3.5°$**.**

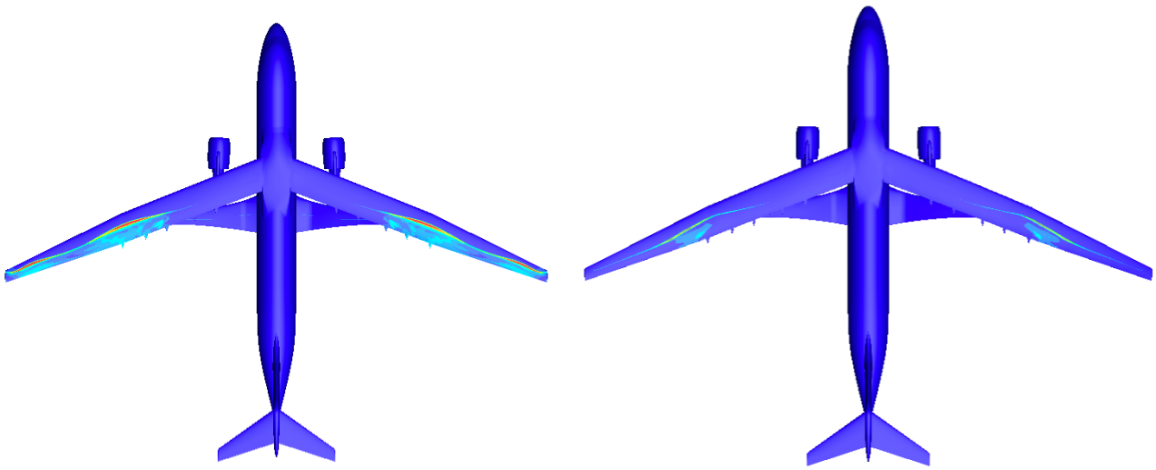

(a) 1g OML (b) Aeroelastic OML

Figure 26 RMS Value of Unsteady Pressure of the Mach 0.8 TTBW 1g OML and Aeroelastic mode at Mach 0.8, h = 40,000ft and angle of attack $4.0°$**.**

(a) Aeroelastic OML

Figure 27 RMS Value of Unsteady Pressure of the Mach 0.8 TTBW Aeroelastic mode at Mach 0.8, h = 40,000ft and angle of attack 4.5°**.**

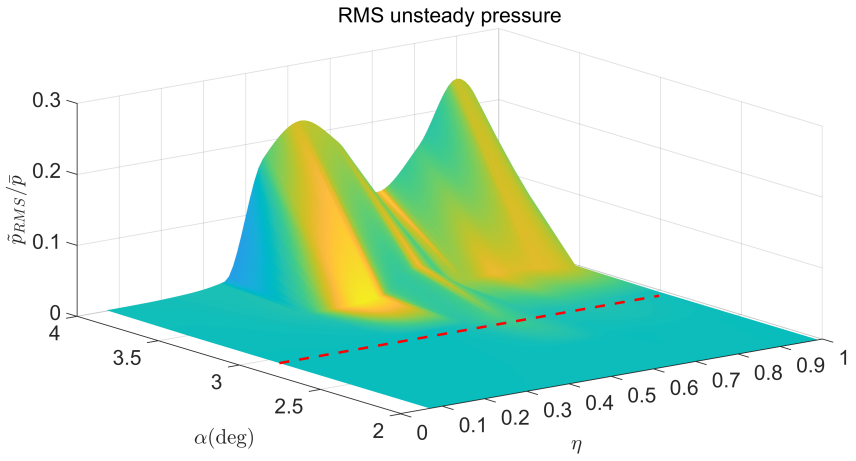

(a) 1g OML

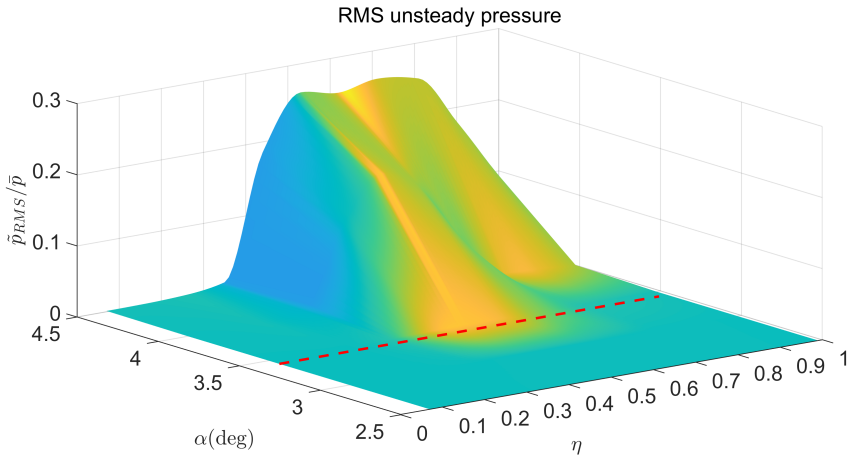

(b) Aeroelastic OML

Figure 28 Peak RMS values of Unsteady Pressure of the Mach 0.8 TTBW 1g OML and Aeroelastic Model at Mach 0.8 and h = 40,000ft.

Conclusions

In this study, we present unsteady DDES buffet simulations of the Mach 0.8 TTBW aeroelastic model using the high-fidelity CFD solver FUN3D. A jig twist optimization is conducted to achieve a flight-optimized jig twist for the flexible Mach 0.8 TTBW aeroelastic model. The DDES simulations indicate that the pitch break occurs at an angle of attack of 2.75° for the 1g OML and 3.2° for the aeroelastic model. The unsteady pressure data suggest a qualitative indication of buffet onset at approximately 3.5° for the 1g OML and 4.0° for the aeroelastic OML. Notably, the pitch break precedes the buffet onset for both models. The unsteady pressure shows that the wing region from the mid-span to the wing tip is predominantly affected by buffeting flow. The aeroelastic deformation of the wing significantly impacts both static pitch stability and buffet onset. The load relief due to aeroelasticity may explain the delay in both pitch break and buffet onset.

Acknowledgment

The authors wish to acknowledge NASA Advanced Air Transport Technology project for the funding support of this work. The authors also acknowledge Boeing Research and Technology and in particular Christopher Droney, Neal

Harrison, Michael Beyar, Eric Dickey, and Anthony Sclafani, along with the NASA technical POC, Gregory Gatlin, for their research conducted under the NASA BAART contracts NNL10AA05B and NNL16AA04B. The research published in this paper is made possible by the technical data and wind tunnel test data furnished under these BAART contracts.

References

[1] Bhatia, M., et. al.. "Structural and Aeroelastic Characteristics of Truss-Braced Wing: A Parametric Study," Journal of Aircraft, Vol 49, No. 1, 2012.

[2] Gundlach, J. F., Tetrault, P. A., Gern, F. H., Nagshineh-Pour, A. H., Ko, A., Schetz, J. A., et. al., "Conceptual Design Studies of a Strut-Braced Wing Transonic Transport," Journal of Aircraft, Vol. 37, No. 6, 2000.

[3] Gur, O., Bhatia, M., Schetz, J.A., Mason, W. H., Kapania, R. K., and Mavris, D. N., "Design Optimization of a Truss-Braced Wing Transonic Transport Aircraft," Journal of Aircraft, Vol. 47, No. 6, 2010.

[4] Xiong, J. and Nguyen, N., "Steady and Unsteady Simulations of Transonic Truss-Braced Wing Aircraft for Flight Dynamic Stability Analysis," AIAA Aviation Conference, AIAA-2022, June 2022.

[5] Nguyen, N. and Xiong, J., "CFD-Based Frequency Domain Method for Dynamic Stability Derivative Estimation with Application to Transonic Truss-Braced Wing," AIAA Aviation Conference, AIAA-2022, June 2022.

[6] Nguyen, N. and Xiong, J., "Frequency Domain Method for Dynamic Control Derivative Estimation with Application to Transonic Truss- Braced Wing," AIAA Aviation Conference, AIAA-2023, June 2023.

[7] Xiong, J. and Nguyen, N., "Simulations of Mach 0.8 Transonic Truss-Braced Wing Aircraft Aerodynamics at High Angles of Attack," AIAA Aviation Conference, AIAA-2023-4528, June 2023.

[8] Biedron, R. T., et al., "FUN3D Manual 13.2,", NASA TM-2017-219661, Aug. 2017

[9] Lee-Rausch, E. M., Hammond, D. P., Nielsen, E. J., Pirzadeh, S. Z., and Rumsey, C. L., "Application of the FUN3D Unstructured-Grid Navier-Stokes Solver to the 4th AIAA Drag Prediction Workshop cases," AIAA Aviation Conference, AIAA-2010-4511, January 2019.

[10] Roe, P. L., "Approximate Riemann Solvers, Parameter Vectors and Difference Schemes,", Journal of Computational Physics, Vol. 46, No. 2, 1980, pp. 357-378

[11] Venkatakrishnan, V., "Convergence to Steady State Solutions of the Euler Equations on Unstructured Grids with Limiters,", Journal of Computational Physics, Vol. 118, No. 1, 1995, pp. 120-130

[12] Spalart, P. R. and Allmaras, S. R., "A One-Equation Turbulence Model for Aerodynamic Flows," AIAA Science and Technology Forum and Exposition, AIAA-1992-0439, January 1992.

[13] Xiong, J., Nguyen, N., and Bartels, R. E., "Jig Twist Optimization of Mach 0.8 Transonic Truss-Braced Wing Aircraft," AIAA Science and Technology Forum and Exposition, AIAA-2023, Jan. 2023.

[14] Xiong, J., Nguyen, N., and Fugate, J., "Investigation of Truss-Braced Wing Aircraft Transonic Wing-Strut Interference Effects Using FUN3D," AIAA Aviation Conference, AIAA-2019-3026, June 2019.

[15] Xiong, J., Nguyen, N., and Bartels, R. E., "Aerodynamic Optimization of Mach 0.8 Transonic Truss-BracedWing Aircraft using Variable Camber Continuous Trailing Edge Flap," AIAA Science and Technology Forum and Exposition, AIAA-2022-0016, Jan. 2022.

[16] Harrison, N. A., Beyar, M. D., Dickey, E. D., Hoffman, K., Gatlin, G.M. and Viken, S. A., "Development of an Efficient Mach=0.80 Transonic Truss-Braced Wing Aircraft," AIAA SciTech Conference, AIAA-2020-0011, January 2020.

[17] Bartels, R. E., Stanford B. K., Waite, J. M., "Performance Enhancement of the Flexible Transonic Truss-Braced Wing Aircraft Using Variable-Camber Continuous Trailing-Edge Flaps," AIAA 2019-0316, June 17-21, 2019, Dallas, Texas